TELLUS

Effect of a wavy wall on the single gyre Munk problem

By FRÉDÉRIC DUPONT[1]* and DAVID N. STRAUB[2], ᅠ[1]*Coastal Ocean Sciences, Bedford Institute of Oceanography, PO Box 1006, Dartmouth, NS, B2Y-4A2, Canada;* [2]*Department of Atmospheric and Oceanic Sciences, McGill University, 805 Sherbrooke W, H3A 2K6, Montréal, Québec, Canada*

ABSTRACT

A spectral element shallow water model with an adaptive triangular mesh is used to examine the effects of basin geometry on the single gyre Munk problem. Specifically, we consider a circular basin shape, with and without the addition of a sinusoidal undulation in the coastline. We are particularly interested in how the curviness of the coastline might effect the well-known tendency of the solution to 'runaway' as the lateral viscous coefficient is made small. Results were dependent on boundary conditions. We consider both no slip and three variants of the free slip condition: zero vorticity at the coast, zero normal derivative of tangential velocity and zero normal flux of tangential momentum. For cases where the coastal undulations were large in amplitude, the no slip and the third free slip condition showed the least tendency towards runaway (i.e. towards developing unrealistically large velocities as the viscous coefficient was made small). In the circular geometry, by contrast, the differences between no slip and free slip were much greater, and of the variants on free slip, the zero vorticity condition showed the least tendency towards runaway. We also show that high-frequency variability (such as Kelvin waves) can differ markedly depending on which of the three free slip variants is used.

1. Introduction

Despite their simplicity, the single layer Stommel and Munk models remain useful reference points in our understanding of mid-latitude gyres. It is widely appreciated, of course, that various features absent in these simple models are essential to a complete picture. For example, the role of baroclinic eddies has been stressed by Rhines and Young (1982) and the role of outcropping isopycnals was emphasized by Luyten et al. (1983). Nonetheless, sometimes it remains instructive to return to the simpler, single layer setting when addressing specific issues pertaining to the dynamics. Here, we consider the combined effect of boundary conditions and an undulating coastline in the non-linear single gyre Munk problem.

Our motivation for focusing on the single gyre non-linear Munk problem is that this represents, in some sense, a worst-case scenario with respect to the problem of inertial runaway. Inertial runaway is the tendency for model solutions to exhibit unrealistically large velocities as frictional parameters, such as the Munk eddy viscosity, are made small. The one layer single gyre problem precludes cross-gyre exchange of vorticity by baroclinic eddies, a process which plays a dominant role in balancing vorticity budgets for individual gyres (Harrison and Holland 1981; Marshall 1984). This lack of exchange creates problems

balancing the vorticity budget and these problems are thought to be one of the root causes of runaway (Ierley and Sheremet 1995; Pedlosky 1996). Another root cause of inertial runaway is thought to be related to energetics (Scott and Straub 1998). Our focus on the Munk problem removes scale-independent energy dissipation by bottom friction from consideration, and this, too, surely exacerbates the tendency towards runaway. Our principal interest here is to focus on another model feature which may play a significant role in helping to curb or slow the runaway process: complexities in basin geometry. Specifically, we consider circular geometries, with and without a sinusoidal wave added to the coastline.

The issue of how a wavy wall might help to curb runaway turns out to be intimately related to the choice of dynamic boundary condition. We consider both slip and no slip, but focus primarily on slip conditions. Slip (or free slip) is normally defined as no normal flow plus one of three obvious choices:

(1)ᅠ the vorticity vanishes at the wall;
(2)ᅠ the normal derivative of the tangential velocity vanishes at the wall;
(3)ᅠ the off-diagonal elements of the symmetric strain tensor (after proper rotation) vanish at the wall.

On a straight wall, conditions 1–3 (hereafter referred to as FS1, FS2 and FS3) are identical. For example, on a meridionally-oriented western boundary, FS1 states that $\partial_x v - \partial_y u = 0$, FS2

*Corresponding author.
e-mail: dupontf@mar.dfo-mpo.gc.ca

states that $\partial_x v = 0$ and FS3 states that $\partial_x v + \partial_y u = 0$.[1] However, because the no normal flow condition would have that $u = 0$ for all y along the boundary, the three conditions are equivalent. This is not the case on a curved boundary. For example, let U and V be the normal and tangential velocity components, corresponding to coordinates n and l. Take (n, l) to be defined as right-handed coordinates with $\hat{\mathbf{n}}$ pointing out of the basin. Furthermore, define the radius of curvature as

$$\frac{\partial \hat{\mathbf{l}}}{\partial l} = -\kappa \hat{\mathbf{n}}. \tag{1}$$

Note that for a circular basin κ is positive and equal to the inverse radius of the basin. Then, the three conditions reduce to

$$\frac{\partial V}{\partial n} + \alpha \kappa V = 0 \tag{2}$$

on the wall. Here, α takes on values of $1, 0$ or -1 for FS1, FS2 and FS3, respectively. For FS1, eq. (2) arises because the vorticity along the boundary can be expressed as

$$\zeta = \partial_x v - \partial_y u = \frac{\partial V}{\partial n} + \kappa V = 0. \tag{3}$$

For FS3, eq. (2) arises because the normal flux of tangential momentum along the boundary can be expressed as

$$(n_x, n_y)\mathbf{S}_1 \begin{pmatrix} l_x \\ l_y \end{pmatrix} = -\frac{\partial V}{\partial n} + \kappa V = 0. \tag{4}$$

To ensure negative definite energy dissipation, one normally requires that no work be done by the stress at the boundary. This is assured under no slip because the velocity vanishes. Under free slip, it is necessary that the normal flux of tangential momentum across the wall vanish. We use the symmetric strain tensor formulation for FS3 and the $\nabla \mathbf{v}$ formulation for FS1, FS2 and no slip (see footnote 1). Because of this, the normal flux of tangential momentum across the wall in the latter cases is given by

$$(n_x, n_y)\mathbf{S}_2 \begin{pmatrix} l_x \\ l_y \end{pmatrix} = -\frac{\partial V}{\partial n}. \tag{5}$$

Hence, using eqs. (4) and (5), and the definitions of the various boundary conditions, we have that the normal flux of tangential momentum vanishes identically for FS2 and FS3, but that it is given by κV for FS1. FS1 can thus be thought of as analogous to partial slip, except that the proportionality 'constant' between the stress and the tangential velocity depends on the curvature of the boundary. For complex geometries, κ takes on both positive

and negative values. In regions where $\kappa < 0$ (e.g. near the tips of peninsulas), the viscous stress will add energy to the fluid. Because of this, for the FS1 condition, we have no a priori guarantee that the viscous terms will provide a net sink of energy. In this paper, we compare results for all three slip conditions with each other as well as with the no slip condition in a mid-latitude ocean gyre setting. We also note that there are a number of numerical subtleties involved in representing complex geometries. Here, we adopt a spectral element (SE) approach.

The paper is organized as follows. In Section 2, we describe the SE model and an automated mesh refinement method that we employ. In Section 3, we present details of the experimental set-up, and the results for a range of viscous coefficients and amplitudes of the coastline undulations. We conclude briefly in Section 4.

2. Model

We consider the reduced gravity shallow water equations. These equations, rather than the quasigeostrophic (QG) equations, were chosen because $O(1)$ Rossby numbers are anticipated. A reduced gravity version was preferred, because the numerics then allow for a larger time-step. Forcing is by a zonal wind stress, $\tau^x = \tau_0 \sin(\pi y/L)$. This is represented as a body force distributed over the active layer. The equations then become

$$\frac{\mathrm{D}}{\mathrm{D}t}u - (f_0 + \beta y)v = -g'\frac{\partial \eta}{\partial x} + \frac{\tau^x}{\rho_0 \eta} + F_u$$

$$\frac{\mathrm{D}}{\mathrm{D}t}v + (f_0 + \beta y)u = -g'\frac{\partial \eta}{\partial y} + F_v \tag{6}$$

$$\frac{\mathrm{D}}{\mathrm{D}t}\eta + \eta \nabla \cdot \mathbf{u} = 0.$$

Here, η is the layer thickness, F_u and F_v are the viscous forces and g' is the reduced gravity where the bottom layer is assumed motionless. Model parameters are presented in the nomenclature section.

The numerical formulation of the viscous forces varies depending on the choice of boundary condition. Analytically,[2] F_u and F_v are given by

$$F_u = A\nabla^2 u$$
$$F_v = A\nabla^2 v \tag{7}$$

---

[1] The viscous force can be written as the divergence of $\mathbf{S}$, where $\mathbf{S}$ is either the symmetric strain tensor ($\mathbf{S}_1$) or $\nabla \mathbf{v}$ ($\mathbf{S}_2$). More precisely,

$$\mathbf{S}_1 = \begin{bmatrix} 2\partial_x u & (\partial_x v + \partial_y u) \\ (\partial_x v + \partial_y u) & 2\partial_y v \end{bmatrix} \quad \text{or} \quad \mathbf{S}_2 = \begin{pmatrix} \partial_x u & \partial_x v \\ \partial_y u & \partial_y v \end{pmatrix}.$$

Mathematically, these two formulations are equivalent in the limit of non-divergent flow, but differ here because the horizontal divergence is non-zero. We use the symmetric strain tensor formulation when the third free slip boundary condition is used.

[2] As pointed out by an anonymous reviewer, it would have made more sense to write the viscous terms as $(1/\eta)\nabla \cdot (\eta \mathbf{S})$, because this formulation has better energy conservation properties. An extra set of runs for FS2 was performed and shows marginal changes if a more consistent energy viscous tensor is used instead. We nonetheless expect more significant differences to arise as layer thickness variations approach the $O(1)$ limit, i.e. close to the transition to the high energetic branch that characterizes the inertial runaway. See also Gent (1993) and Shchepetkin and O'Brien (1996) for a more detailed discussion on appropriate forms of the viscous tensor.

except under FS3, for which

$$F_u = A(\partial_x S_{111} + \partial_y S_{121})$$
$$F_v = A(\partial_x S_{112} + \partial_y S_{122}). \tag{8}$$

For no slip and FS2, $\nabla^2 \mathbf{v}$ is discretized directly. For FS1, we use the vorticity-divergence formulation (Madec et al. 1991)

$$F_u = A(\partial_x \delta - \partial_y \zeta)$$
$$F_v = A(\partial_y \delta + \partial_x \zeta). \tag{9}$$

where $\delta = \partial_x u + \partial_y v$ is the divergence and $\zeta = \partial_x v - \partial_y u$ is the relative vorticity. Also for FS1, the advective terms in the momentum equations are also split between a vorticity term and a gradient term. It must be stressed that the divergence-vorticity form is only used here for convenience of numerical implementation. Except for the boundary condition, the model with FS1 is identical to that with FS2.

2.1. Discontinuous spectral element model

The curvilinear geometry poses various numerical problems that make the more commonly used finite difference (FD) methods somewhat problematic (see, for example, Adcroft and Marshall 1998; Dupont et al. 2003). We choose instead to use a triangular discontinuous SE method, and summarize its main characteristics below. A more complete description can be found in Lomtev and Karniadakis (1999) and Dupont and Lin (2003).

In essence, the SE method is a high-order finite element (FE) method where a basis of polynomials of fixed order spans the element. As with the spectral method, the accuracy of the SE method increases exponentially with increasing polynomial order. However, the SE method offers more flexibility in geometrical representation. Moreover, contrary to the spectral method where Gibbs oscillations are prone to occur in underresolved regions, one can easily increase the number of elements (*h*-refinement) in the underresolved regions in the SE method. Using a polynomial order greater than two, we can also expect that the SE method is more accurate than conventional second-order FD or FE methods with linear basis functions, and that the convergence of the solution with increasing resolution is much faster.

Previous applications of the SE method to ocean modelling have used quadrangles, rather than triangles (Ma 1993; Iskandarani et al. 1995). Using quadrangles, it is relatively easy to construct an orthogonal basis of cardinal functions which renders trivial the matrix problem to be solved, provided the equations are prognostic and solved explicitly in time (e.g. leapfrog, Adams–Bashforth, Runge–Kutta). In this case, the modal coefficients associated with each basis function are also the actual physical values. The computation of non-linear terms is therefore straightforward and does not require transfer from polynomial space to physical space. Triangles, on the other hand, offer more flexibility in the discretization of irregular domains.

Furthermore, automatic and local conforming mesh refinement is straightforward in triangular meshes. This is generally more difficult for quadrilateral meshes.[3] A problem with triangles, however, is that there is no orthogonal basis of cardinal functions in triangles.[4] Because of this, the computation of non-linear terms requires a tedious transfer from the spectral coefficients to values at physical Gauss-like points, and back to the spectral space.

Cockburn et al. (1990) introduced a discontinuous Galerkin formulation which leads to a local matrix problem in each element-triangle. This is only possible if all the equations are prognostic (as they are for shallow water models) and treated explicitly in time. The use of discontinuous basis functions may introduce a slight loss in truncation order, but appears to be stable (no development of spurious pressure modes), even though the same set of basis functions is used for the velocity and pressure. Thus, in contrast to elements with continuous basis functions, the discontinuous SE method does not require that the LBB condition (Ladyzhenskaya 1969; Babuska 1971; Brezzi 1974) be respected. Furthermore, it allows for an easy implementation of a time-variable triangular mesh, such as introduced in Dupont and Lin (2003). Thus, although triangular elements are less optimal for computations than quadrangles we nonetheless prefer them for their higher degree of flexibility when discretizing an irregular domain and for the small effort of coding required for introducing mesh adaptivity in the discontinuous Galerkin formulation.

2.2. Basis functions

In our model, based on Lomtev and Karniadakis (1999), the matrix problem to be solved in each element is small enough (the polynomial order is fixed at 5) that the constraint of orthogonality over the set of polynomials is less stringent. Thus, we introduce an even simpler set of basis functions compared to Lomtev and Karniadakis (1999). That is, we use a set of products of Legendre polynomials with a triangular truncation (and no use of degenerate point or collapse local coordinates)

$$\phi_i(\xi_1, \xi_2) = L_l(\xi_1) L_k(\xi_2), l + k \leq n_c, \tag{10}$$

where n_c is the maximum order of the polynomials, ξ_1 and ξ_2 are the local coordinates inside the element (Fig. 1) and i is indexed as l runs from 0 to n_c and k runs from 0 to $n_c - l$. The solution can be expressed inside the element j by

$$f(\xi_1, \xi_2, t)^j = \sum_i a_{ij}(t) \phi_i(\xi_1, \xi_2, t). \tag{11}$$

---

[3]One exception is the use of non-conforming quadrilaterals (Mavriplis and Hsu 1997) which allows for direct subdivision of one quadrilateral without any change to the rest of the mesh.

[4]Some orthogonal bases exist (Lomtev and Karniadakis 1999) but they are not cardinal. Taylor and Wingate (2000) introduced a collocation method based on the Fekete points on the triangle at the expense of some accuracy.
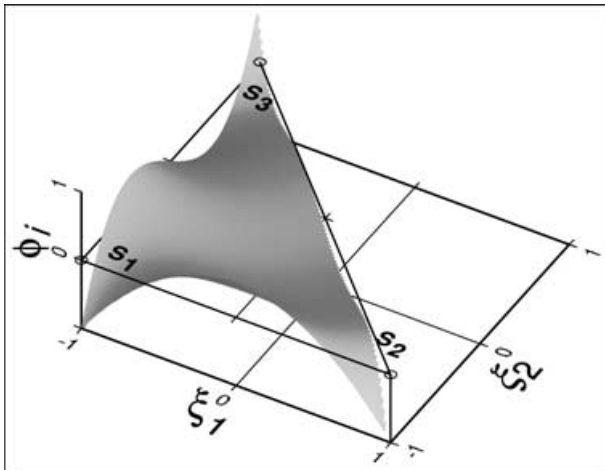
Fig 1. $S_{i=1..3}$ are the vertices of the triangles oriented anticlockwise. (ξ_1, ξ_2) are the local coordinates in a given triangle. As an example, $\Phi_i = L_2(\xi_1) L_3(\xi_2)$ is plotted. Φ_i is quadratic along $\xi_2 = -1$, cubic along $\xi_1 = -1$ and quintic along $\xi_1 + \xi_2 = 0$.

For implementation of the various boundary conditions, the variable under interest is projected onto a modified set of basis functions. The latter is straightforward modification of the original set so that all basis functions are identically zero along the lateral wall (see Dupont and Lin 2003, for more details).

The discontinuous SE method leads to a flux formulation through the edges of each element. The boundary values of these fluxes have be to computed in terms of the neighbouring elements. We choose to define the boundary value as the mean value of both sides of a face, i.e.

$$f_{\text{bd}}(\xi_{\text{bd}}) = 0.5 \times \left[f^{j_1}(\xi_{\text{bd}}) + f^{j_2}(\xi_{\text{bd}}) \right], \tag{12}$$

where f is any function, ξ_{bd} is a coordinate running along the considered face of an element and j_1 and j_2 are the indices of the two adjacent elements to this face. The subscript 'bd' for each variable refers to the value of the variable along the interelement edge. It is also possible to introduce an upwind formulation based on a local Riemann problem for the computations of the fluxes (Lomtev and Karniadakis 1999). This was not pursued though because oceanic flows are typically subcritical.

A final characteristic of our SE model is that the elements along the domain boundary are curved following a parabolic profile. This introduces a transformation Jacobian matrix for these elements when computing, for instance, the mass matrix or the non-linear terms. The number of Gaussian points has therefore to be accordingly augmented in these elements for the computation of the matrices to be exact considering the maximal polynomial order used.[5]

---

[5]The curved profile of the boundary elements is only quadratic so as to prevent an unreasonable increase in computations.

2.3. Adaptivity

Large discontinuities in the vorticity field developed in some of our preliminary simulations. This was especially problematic between elements close to bumps 1 and 2 (see Fig. 2). Some of these discontinuities are associated with the piecewise boundary parabolas near inflection points along the coastline, where cubic polynomials would be more adequate. Therefore, following preliminary runs, we redesigned the mesh with more points along the western bumps, and slightly more points in the interior. This led to considerable improvement; however, further refinement was needed, especially in proximity of bumps 2 and 3. To accomplish this, we used an adaptive strategy similar to that developed in Dupont and Lin (2003). We have a certain level of liberty in the choice of the fields and the parameters controlling the selection of the elements to be refined. Dupont and Lin (2003) use the primitive variables for controlling the level errors. We choose instead to use the vorticity. Because the vorticity is a field one order higher relative to the velocity, it should follow that if the vorticity is correctly resolved, then the lower-order fields should be as well. We found that this approach was reliable by testing the adaptive strategy in a simpler experiment (not shown). Unfortunately for geometry V (see below), we could not afford the computational cost for more than one adaptive cycle. As we will see below, the main features of the circulation appear to have converged, with some exceptions that appear to be of relatively minor importance. After one cycle (Fig. 3), the refined elements are concentrated along the tip of bump 2 and less near bump 1. Of course, the refinement has a cost. The simulation on the refined mesh is about four times more expensive than that on the original mesh, mainly due to time-step limitations that affect the entire domain.

3. Experimental results

We consider the single gyre Munk problem in a circular domain of radius 500 km perturbed by the addition of a sine wave along the coast. The wavelength of the sinusoidal undulations in the coastline is 1/16 of the circumference of the basic circular domain, and its amplitude ranges from 0 to 100 km. The minimum radius of curvature takes on values of 500, 160, 80, 40 and 20 km for geometries I–V, respectively. We will limit ourselves, however, to show and discuss circulations in geometries I, III and V. As mentioned above, wind forcing takes the form of a sinusoidal eastward stress, i.e. as in the standard single gyre problem. The inertial layer thickness is worked out to be about 28 km. Two values of the eddy viscosity were mainly considered ($\nu = 700$ and $100 \text{ m}^2 \text{ s}^{-2}$), so that the Munk layer width ranged from about 35 to 18 km. The boundary layer Reynolds number, Re, equal to the cube of the inertial boundary layer thickness divided by the Munk boundary layer thickness (e.g. Pedlosky 1996) thus ranges from 0.5 to 3.5. For comparison, Scott and Straub (1998) reached values of about 35 for double gyre steady
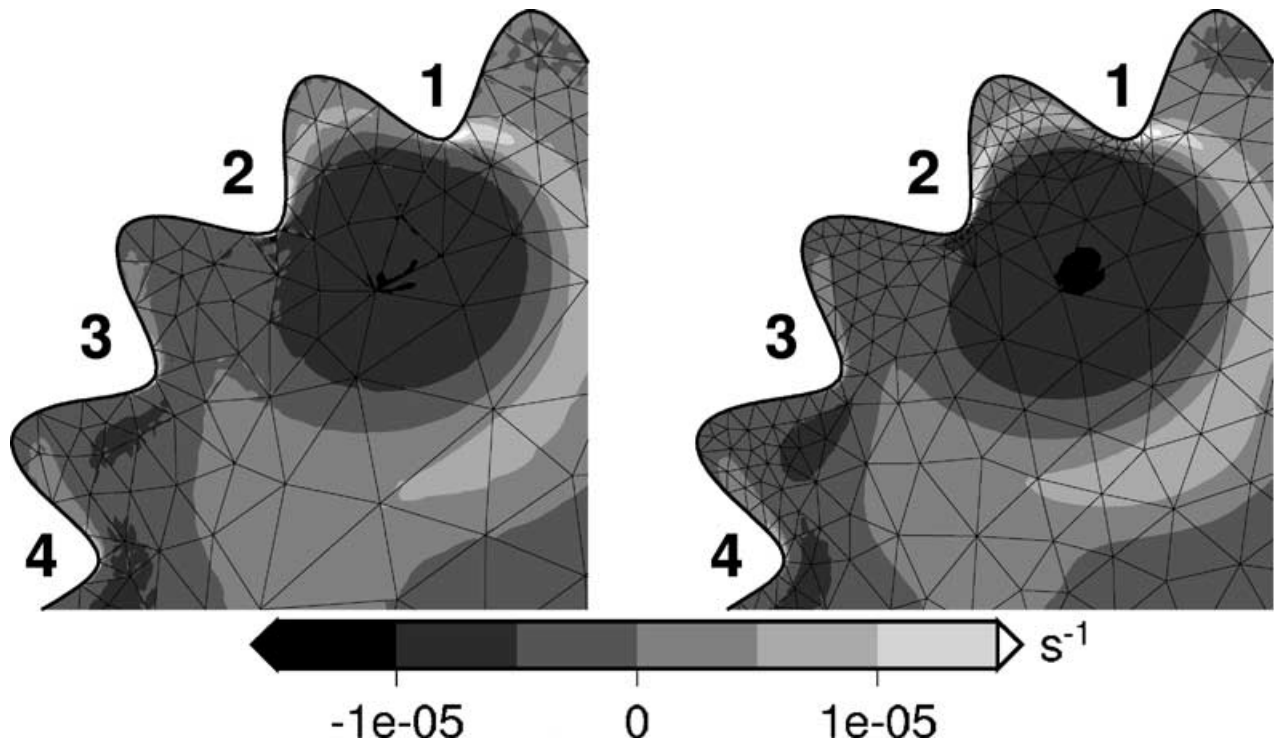
Fig 2. Mean vorticity (left) before and (right) after adaptive mesh refinement for geometry V, *Re* = 3.5 using FS2. The numbers are the bumps of interest.
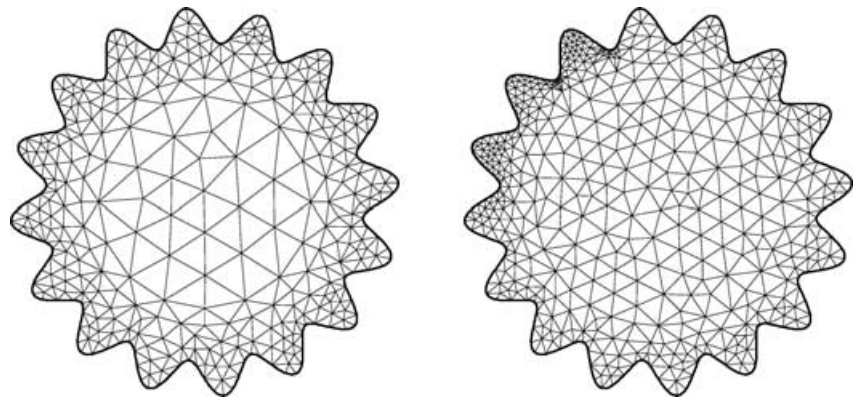

Fig 3. Mesh for the original and the refined runs.

circulations with a (time-independent) QG model. Although, our maximum value is somewhat lower, in the context of the single gyre problem, 3.5 can be considered 'moderately large' value. For example, in the rectangular-basin version of the problem, basin-filling gyres develop under slip conditions for Reynolds numbers as low as *Re* = 2 (Ierley and Sheremet 1995). Note that non-linear wind-driven circulations in the circular geometry were first investigated by Beardsley (1973) and Briggs (1980), and more recently by Kiss (2002).

Because we are interested in the time mean states of the circulation, when possible, we performed 6-yr averages of the fields after a statistical steady state has been reached. The length of this period was limited by computer resources. It is slightly short because six years represent only twice the time for a Rossby wave to cross the basin. However, we do not believe that these results would significantly differ for longer averaging periods.

Figures 4–7 show the different statistical mean circulations obtained for the various geometries and boundary conditions. An 'X' denotes when a statistical mean could not be reached. Such is the case when the solution jumps to the high energetic branch. When this occurs, the tilt in the interface height field implied by geostrophic balance leads to zero layer thicknesses, at which point the integration is halted. Figure 8 synthesizes the results by showing kinetic energy as a function of *Re*. The main result, then, is that the presence of undulations along the coastline
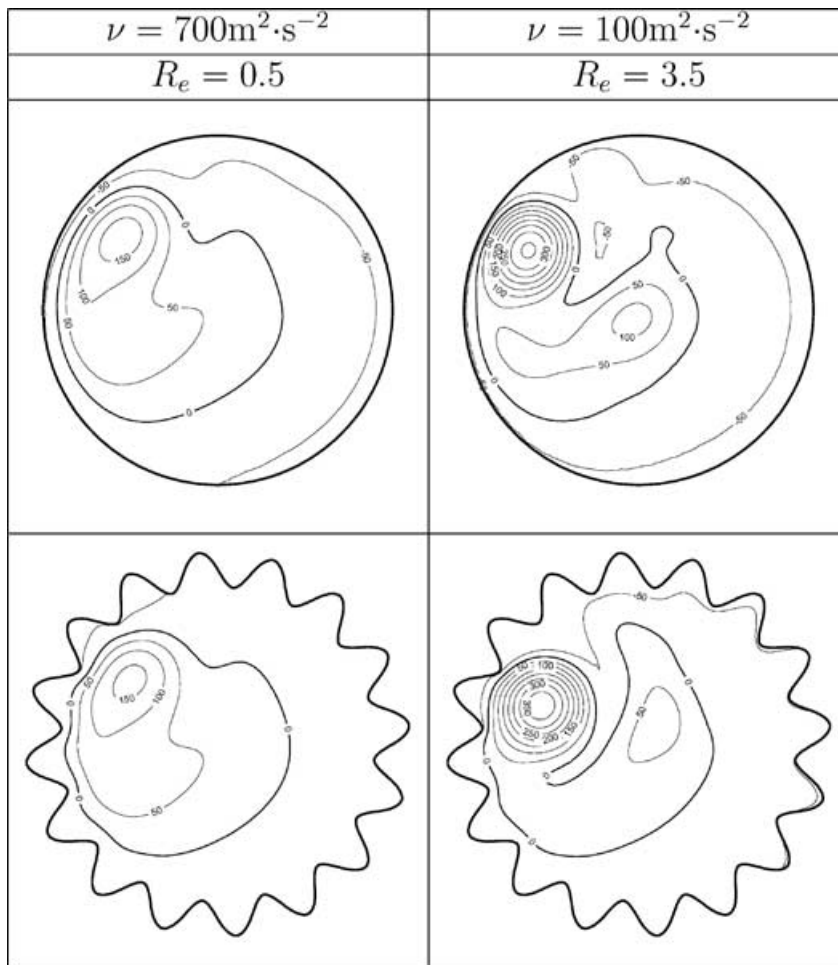
Fig 4. Mean elevation fields using the SE model. When no steady state could be reached because the solution jumps to the high energetic branch, an 'X' is drawn instead. The dynamical boundary condition employed is no slip boundary conditions. Only results for geometries I and V and for $Re = 0.5$ and 3.5 are shown.

helps to slow the runaway process under free slip conditions. An exception to this rule is the FS1 condition, for which the solution has 'run away' in our higher Re simulations, even in the case where geometry V was used. It appears, however, that a fairly small local radius of curvature in the coastline is needed to obtain reasonable solutions for larger Re under slip boundary conditions.

The no slip and FS1 boundary conditions were the least sensitive to the amplitude of the bumps. No slip generally shows a weaker tendency towards runaway, whereas FS1 generally shows a strong one. However, there was also considerable variability between the various geometries. For example, of the three free slip conditions, FS3 shows the least tendency towards runaway in geometry V, but the strongest in geometry I. For geometry V, the strength of the recirculation under FS3 is similar to the strength of the recirculation under the no slip condition. By contrast, for the same geometry FS2 and FS1 show stronger recirculations (more tendency towards runaway). Thus, the slip boundary condition that most exacerbates the runaway problem in a circular domain is also the one that best curbs the problem in geometry V.

These results might be understood qualitatively as follows. The no slip boundary condition can be obtained as a special limit of the partial slip condition. On a straight wall, partial slip implies

$$\frac{\partial V}{\partial n} - aV = 0. \tag{13}$$

Following our sign convention, a northward flowing western boundary current corresponds to $V < 0$. The limit $a \to 0$ corresponds to free slip, $a > 0$ is a sort of 'super-slip' (with $\partial V/\partial n < 0$; the magnitude of V increasing towards the boundary in the boundary layer) and $a < 0$ gives a behaviour closer to no slip (with $\partial V/\partial n > 0$; the magnitude of V decreasing towards the boundary). No slip corresponds to $a \to \infty$. Referring to eq. (2), we see that positive $\alpha\kappa$ should lead to behaviour similar to that of no slip, whereas negative $\alpha\kappa$ acts to increase the 'slipperiness' of the wall. In a circular domain, κ is positive. Hence, for FS1, $\alpha\kappa > 0$ and, for FS3, $\alpha\kappa < 0$. This is consistent with runaway being more prevalent under FS3 than under FS1 for the circular basin case. In the presence of large amplitude bumps along the wall (e.g. geometry V), the part of the boundary coming into
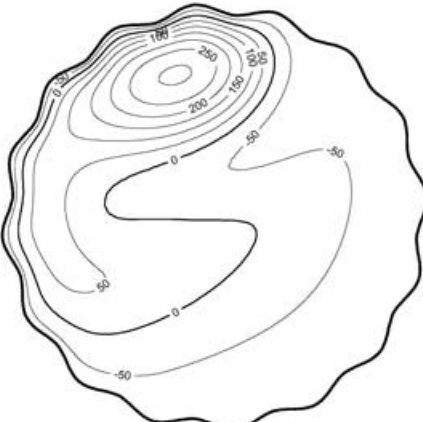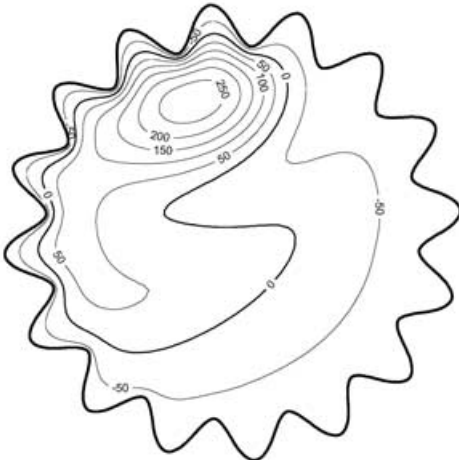
$\nu = 700\mathrm{m}^2\cdot\mathrm{s}^{-2}$	$\nu = 100\mathrm{m}^2\cdot\mathrm{s}^{-2}$
$R_e = 0.5$	$R_e = 3.5$

Fig 5. As for Fig. 4 but for FS1 boundary conditions. Only results for geometries I, III and V and for $Re = 0.5$ and 3.5 are shown.

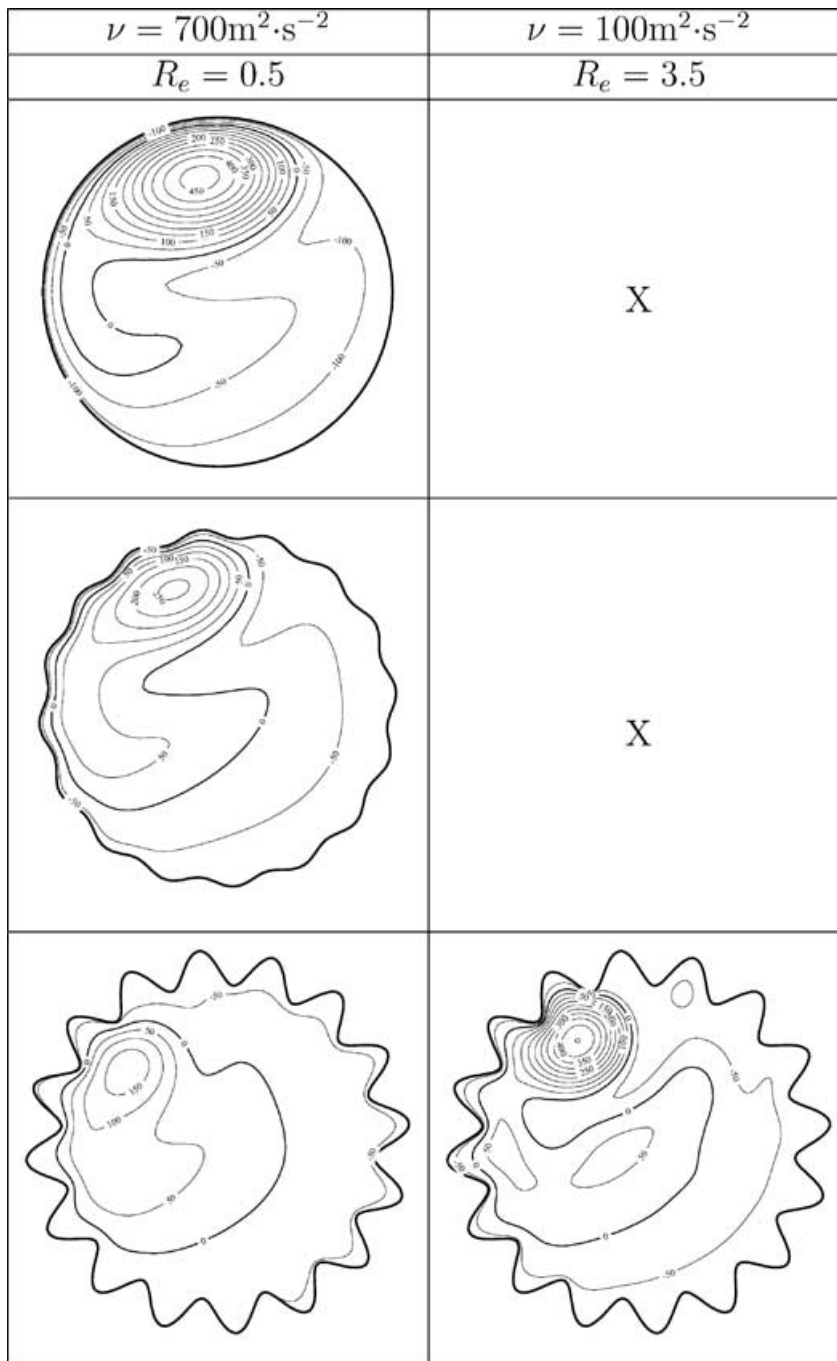| $\nu = 700\mathrm{m}^2{\cdot}\mathrm{s}^{-2}$	$\nu = 100\mathrm{m}^2{\cdot}\mathrm{s}^{-2}$
$R_e = 0.5$	$R_e = 3.5$

Fig 6. As for Fig. 5 but for FS2.

direct contact with the recirculation is near the tips of the bumps, where $\kappa < 0$. Hence, the situation is reversed, and FS3 behaves more like the no slip condition. It is surprising, however, that FS3 actually yields solutions that are less energetic than those obtained using no slip. We do not as yet have a clear explanation as to why this should be the case.

Figure 9 shows the relative vorticity for geometry V and for different Reynolds numbers and boundary conditions. One no-

table feature is the very small length-scales which develop close to the tip of the bumps. Because of this, dynamical processes close to the tip are rather complex, irregular and difficult to resolve using a high-order numerical formulation. The use of a discontinuous SE formulation seems to be of some help in that the irregularities are not propagated to neighbouring elements. This generation of positive vorticity at the boundary is typical under no slip conditions, but does not typically occur as readily
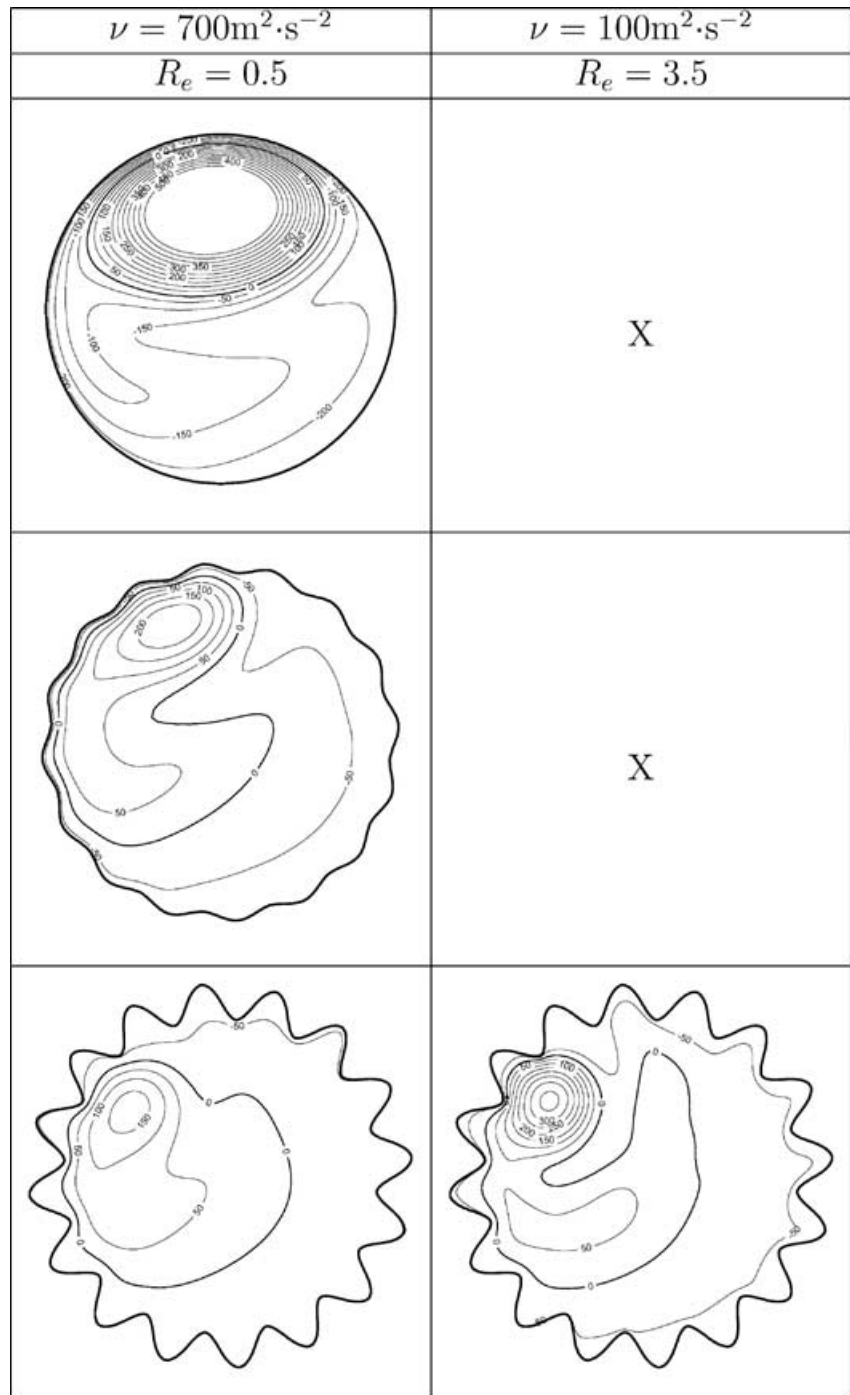
Fig 7. As for Fig. 5 but for FS3.

under free slip, except, as here, in association with curvature in the coastline. Filaments of positive vorticity generated this way become advected downstream and sometimes enter the recirculation zone. This then helps to balance its vorticity budget and, by extension, to slow the runaway process. Surprisingly though, this generation of positive vorticity appears to be more prevalent under FS2 than under FS3. In fact, the vorticity field under FS2 matches closely the structure of vorticity under no slip. The peaks have similar amplitude and the wall of positive vorticity surrounding the recirculation is very similar in both cases. The fact that this process does not occur under FS1 follows by definition of FS1, i.e. because large vorticities on the wall are required. This helps explain why the runaway in the presence of irregular coastlines is stronger under FS1.
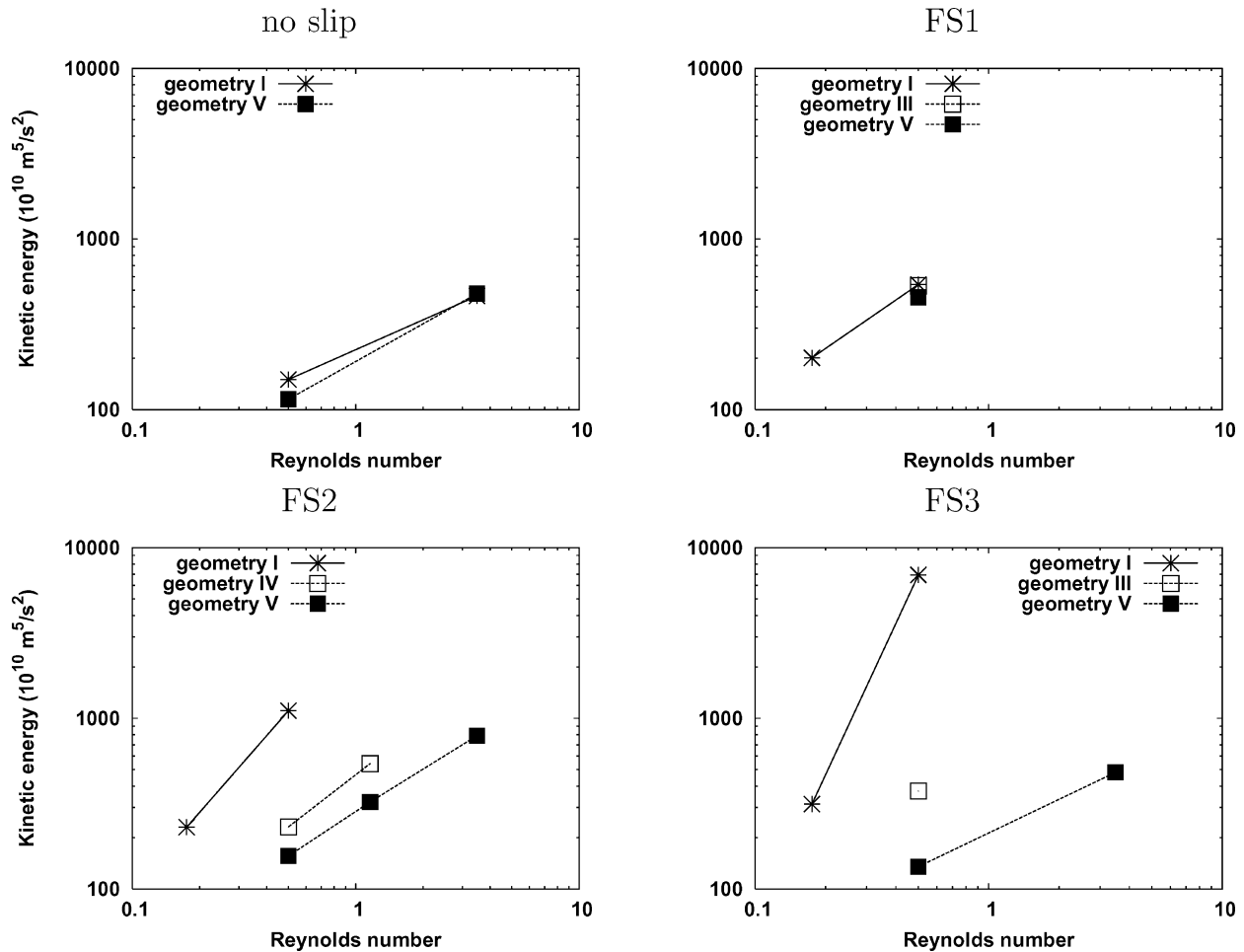
Fig 8. Kinetic energy of time-mean state as a function of *Re* for all four boundary conditions.

We now focus on the transients in the high Reynolds number ($Re = 3.5$) geometry V simulations. Figure 10 shows the standard deviation of the elevation field for the FS2 and FS3 cases. The signal is split into high- and low-pass components. The low-passed portion of the signal is broadly similar between the FS2 and FS3 cases. Figures 10b and d show that part of the variance with periods between 0.6 and 17 d is shown. Note that a Kelvin wave (confirmed by a Hovmöller diagram, not shown) is easily identified in the FS2 case, but is nearly absent in the FS3 case. Presumably, this is a consequence of FS3 behaving more similarly to no slip at the tips of the bumps because no slip is much more effective at inhibiting the propagation of Kelvin waves than FS2 (Davey et al. 1983). Of interest (for the FS2 case) is to note how the spatial pattern of the Kelvin waves varies along the basin perimeter as it interacts with the bumps and the mean circulation. A comparison of results with FS2 and FS3 suggests that the excitation of Kelvin waves under FS2 did not markedly affect the strength of the overall circulation.

4. Conclusion

To summarize, we used a SE method with grid refinement to consider the single gyre Munk problem in a basin with undulating walls. With respect to the numerics, we used an adaptive method to assess the level of convergence of the solution. For that purpose, a simulation under the FS2 boundary condition at $Re = 3.5$ in geometry V was run from year 12 on the refined mesh described in Section 2.3. The discontinuities between elements are less severe for the vorticity field on the refined mesh; however, no structural changes were observed. It thus appears that the mean state and the eddy activity are reasonably well resolved. An exception involves the Kelvin waves along the boundary, for which a doubling of the amplitude was observed with the increased resolution (not shown).

With respect to the dynamics, the main result was that increased irregularities of the coastline slow down (but probably do not prevent entirely) the inertial runaway of the solution with decreasing eddy viscosity for nearly all free slip boundary
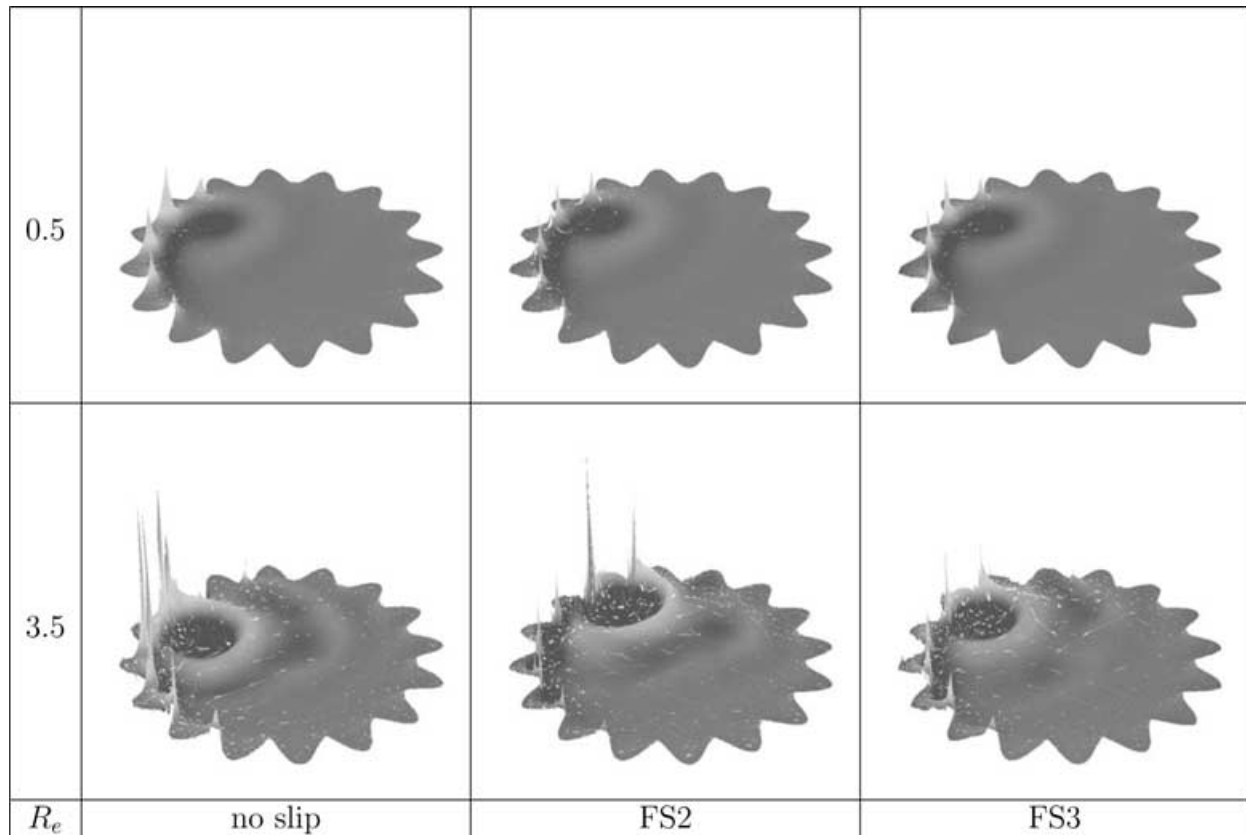
Fig 9. Mean vorticity field in geometry V for no slip, FS2 and FS3 and two Reynolds numbers. The influence of the bumps is clearly seen by the abrupt jump in the vorticity field.

conditions used in this study. One notable exception, however, is the use of FS1 (free slip defined by vanishing vorticity at the walls) for which the inertial runaway is usually the most problematic. Circulations with FS1 are rather insensitive to the basin geometry, as are those with no slip. Circulations with FS2 and FS3 did slow down when bumps were added to the problem, but they did so to varying degrees. Specifically, bumps led to a more marked slowing of the circulation under the FS3 condition. This is because FS3 behaves locally in a manner similar to no slip near the tips of the bumps, where the curvature was large and negative. For cases with smaller amplitude bumps, the curvature of the coastline was generally positive or only weakly negative. Under these conditions, the FS2 condition led to less energetic circulations. This process of slowing down the circulation is achieved in association with the production of thin vorticity filaments (with cyclonic vorticity for the case of anticyclonic forcing that we considered). These peel off from the wall and eventually mix into the anticyclonic vorticity of the recirculation zone. The width of these filaments is clearly limited by the model viscosity.

A shallow water model was chosen (over a QG model) for this study because $O(1)$ Rossby numbers were anticipated. In our larger Re simulations, variability in frequency bands cor-

responding to inertio-gravity waves and to Kelvin waves was observed. It is not clear, however, that these play an important role in the overall energetics. Specifically, there was no obvious correlation between the level of inertio-gravity wave energy and the overall strength of the circulation. Finally, we wish to stress that we purposefully concentrated on the very simple case of a homogeneous, shallow water layer of fluid. Surely, effects absent in our model (topography, baroclinicity, etc.) play important roles in the more complete picture.

5. Appendix: Nomenclature

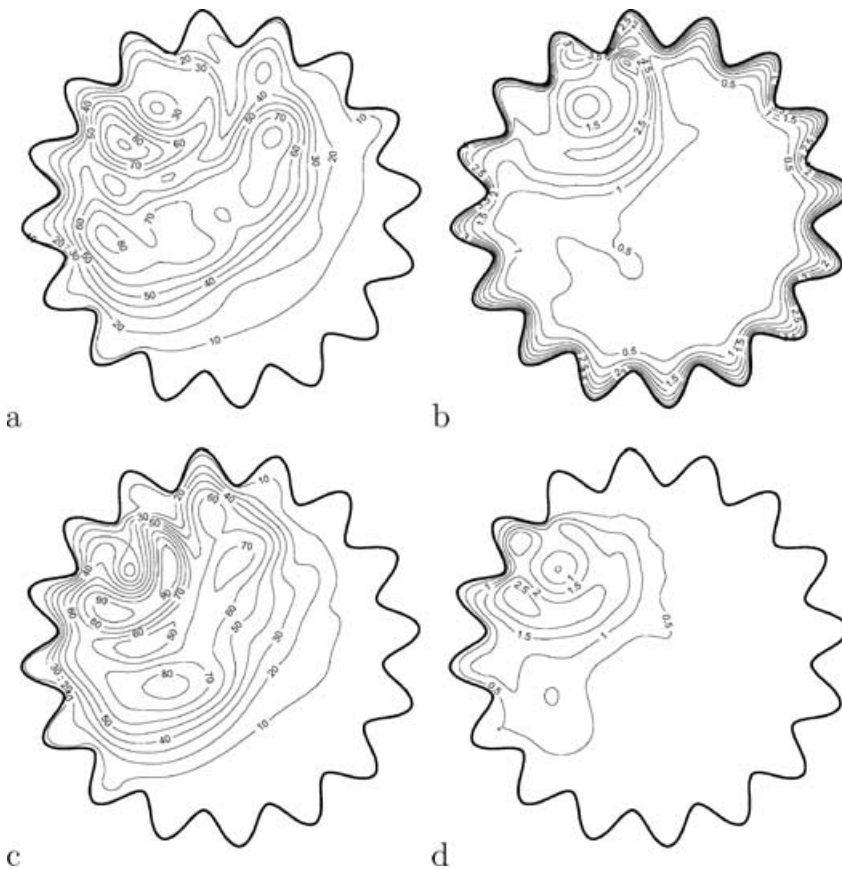|	
x, y	coordinate system (east-north-upward)
$\mathbf{v} = (u, v)$	horizontal velocity vertically averaged
η	layer thickness
$\nabla = (\partial_x, \partial_y)^T$	gradient operator
$f = f_0 + \beta y$	Coriolis parameter varying with latitude
ν	dynamic eddy viscosity
g'	reduced gravity acceleration
$\tau = (\tau_x, \tau_y)$	wind stress in m^2 s^{-2}
$L_x = L_y = 1000$ km	length of the basin

Fig 10. Mean standard deviation of the elevation for frequencies with period above (a) and below (b) 17 d for FS2. (c) and (d) are similar to (a) and (b) but for FS3.

References

Adcroft, A. and Marshall, D. 1998. How slippery are piecewise constant coastlines in numerical ocean models. *Tellus* **50A**, 95–108.

Babuska, I. 1971. Error bounds for finite elements methods. *Numer. Math.* **16**, 322–333.

Beardsley, R. C. 1973. A numerical model of the wind-driven ocean circulation in a circular basin. *Geophys. Fluid Dyn.* **4**, 211–241.

Brezzi, F., 1974. On the existence, uniqueness and approximation of saddle point problems arising from Lagrangian multipliers. *RAIRO, Anal. Num.* **8**(R2), 129–151.

Briggs, W. L. 1980. A new class of steady solutions of the barotropic vorticty equation. *Dyn. Atmos. Oceans* **4**, 67–99.

Cockburn, B., Hou, S. and Shu, C.-W. 1990. TVB Runge–Kutta local projection discontinuous Galerkin finite element method for conservation laws IV: the multidimensional case. *Math. Comput.* **54**, 545–581.

Davey, M. K., Hsieh, W. W. and Wajsowicz, R. C. 1983. The free Kelvin wave with lateral and vertical viscosity. *J. Phys. Oceanogr.* **13**, 2182–2191.

Dupont, F. and Lin, C. A. 2004. The adaptive spectral element method and comparisons with more traditional formulations for ocean modelling. *J. Mar. Atmos. Technol.* **21**, 135–197.

Dupont, F., Straub, D. N. and Lin, C. A. 2003. Influence of a step-like coastline on the basin scale vorticity budget of mid-latitude gyre models. *Tellus* **55A**, 255–272.

Gent, P. R. 1993. The energetically consistent shallow water equations. *J. Atmos. Sci.* **50**, 1323–1325.

Harrison, D. E. and Holland, W. R. 1981. Regional eddy vorticity transport and the equilibrium vorticity budgets of a numerical model ocean circulation. *J. Phys. Oceanogr.* **11**, 190–208.

Ierley, G. R. and Sheremet, V. A. 1995. Multiple solutions and advection-dominated flows in the wind-driven circulation. Part I: slip. *J. Mar. Res.* **53**, 703–738.

Iskandarani, M., Haidvogel, D. B. and Boyd, J. P. 1995. A staggered spectral element model with application to the oceanic shallow water equations. *Int. J. Numer. Methods Fluids* **20**, 393–414.

Kiss, A. E. 2002. Potential vorticity "crisis", adverse pressure gradient, and western boundary current separation. *J. Mar. Res.* **60**, 779–803.

Ladyzhenskaya, O. A. 1969. *The Mathematical Theory of Viscous Incompressible Flow*. Gordon and Breach, London.

Lomtev, I. and Karniadakis, G. 1999. A discontinuous Galerkin method for the Navier–Stokes equations, *Int. J. Numer. Methods Fluids* **29**, 587–603.

Luyten, J. R., Pedlosky, J. and Stommel, H. 1983. The ventilated thermocline, *J. Phys. Oceanogr.* **13**, 292–309.

Ma, H., 1993. A spectral element basin model for the shallow water equations. *J. Comput. Phys.* **109**, 133–149.

Madec, G., Chartier, M., Delecluse, P. and Crepon, M. 1991. A three-dimensional study of deep-water formation in the northwestern mediterranean sea. *J. Phys. Oceanogr.* **21**, 1349–1371.

Marshall, J. C. 1984. Eddy mean flow interaction in a barotropic ocean model. *Q. J. R. Meteorol. Soc.* **110**, 573–590.

Mavriplis, C. and Hsu, L.-C. 1997. A two-dimensional adaptive spectral element method. In: *13th AIAA Computational Fluid Dynamics Conference*, American Meteorological Society, Snowmass, CO.

Pedlosky, J., 1996. *Ocean Circulation Theory*. Springer-Verlag, Heidelberg.

Rhines, P. B. and Young, W. R. 1982. Homogenization of potential vorticity in planetary gyres. *J. Fluid Mech.* **122**, 347–367.

Scott, R. B. and Straub, D. N. 1998. Small viscosity behaviour of a homogeneous, quasi-geostrophic, ocean circulation model. *J. Mar. Res.* **56**, 1225–1258.

Shchepetkin, A. F. and O'Brien, J. 1996. A physically consistent formulation of lateral friction in shallow-water equation ocean models. *Mon. Wea. Rev.* **124**, 1285–1300.

Taylor, M. and Wingate, B. 2000. A generalized diagonal mass matrix spectral element method for non-quadrilateral elements. *Appl. Numer. Math.* **33**, 259–265.